Journal of Materials Chemistry

Cite this: J. Mater. Chem., 2012, 22, 18463

www.rsc.org/materials

PAPER

Structural, electronic band transition and optoelectronic properties of delafossite $CuGa_{1-x}Cr_xO_2$ ($0 \leq x \leq 1$) solid solution films grown by the sol–gel method

Meijie Han, Kai Jiang, Jinzhong Zhang, Wenlei Yu, Yawei Li, Zhigao Hu* and Junhao Chu

Received 13th May 2012, Accepted 19th July 2012
DOI: 10.1039/c2jm33027j

Pure phase $CuGa_{1-x}Cr_xO_2$ ($0 \leq x \leq 1$) films were prepared on (001) sapphire substrates by the sol–gel method. The structure, vibration modes, and compositions of the films were analyzed by X-ray diffraction, scanning electron microscopy, Raman spectroscopy, and X-ray photoelectron spectroscopy. It was found that the Cr-substituting induced the increase of the film's roughness, changed the film's internal structure, and made more crystal defects and grain boundaries. Due to the interatomic potential becoming weaker between Cu and O atoms with increasing the Cu–O bond length, the peak positions of the A_{1g} and A_g phonon modes shifted toward a lower frequency with increasing x. The optical transmittance of the films approached about 60–80% in the visible region and the values of the direct band gap linearly decrease from 3.56 to 3.09 eV with increasing x. The Cr-introduction effects on the electronic band transition have been investigated in detail. The new energy state located at 0.17 eV above the top of the valence band is observed in the $CuGa_{0.8}Cr_{0.2}O_2$ film, which can be derived from the defect energy level. It can induce the increment of the hole in the valence band, contribute to the electrical conductivity, and lower the thermal activation energy. Moreover, the $CuGa_{0.8}Cr_{0.2}O_2$ film is found to be of the larger electrical conductivity of 0.071 S cm^{-1} at room temperature, which shows the promising application values, as compared to other $CuGa_{1-x}Cr_xO_2$ films.

1 Introduction

Transparent conductive oxides (TCOs) have attracted much attention due to their functional combination of transparency and electrical conductivity, which are widely used as transparent electrodes in flat panel displays, light-emitting diodes, laser diodes, solar cells, functional windows, touch panels, UV-detectors, and other technologies.[1–3] Whereas most of the well-known TCOs such as In_2O_3:Sn,[4] ZnO:Al,[5] and SnO_2:F[4] are n-type materials, applications where TCOs work as active devices require both transparent n-type and p-type materials. In recent years, the reports on growing p-type ZnO layers and fabrications of p–n junctions have been heightened.[6,7] However, for II–IV compound semiconductors including ZnO, the control of the nature of conduction is difficult owing to the "self-compensation" of shallow acceptors resulting from various natural donor defects.[8] The interest in the delafossite family as stable and prototype p-type wide band transparent semiconductors without any doping has been increased since p-type $CuAlO_2$ films have been successfully fabricated.[9] In these delafossite compounds, the hybridization of Cu 3d[10] energy levels in the close energy proximity with O 2p levels increases energy of the valence band maximum and delocalizes hole state to form an intrinsic p-type semiconductor.

The delafossite compound $CuMO_2$ (M = Cr, Al, Ga, Fe, Sc, Y, or lanthanide) is isostructural, which can be visualized as consisting of two alternate layers: a planar layer of Cu cation in a triangular pattern and a layer of edge-sharing MO_6 octahedra flattened with respect to the c-axis.[9,10] The difference of the ionic radius of Cr ($r = 0.52$ Å) and Ga ($r = 0.62$ Å) is relatively small, so the Cr–Ga substituting with each other is easy. Thus, the $CuGa_{1-x}Cr_xO_2$ ($0 \leq x \leq 1$) system can be readily fabricated and may combine the good properties from both the $CuGaO_2$ and $CuCrO_2$ material. For example, the work of Ueda *et al.*[11] shows the high optical transparency (~80%) in the visible region for $CuGaO_2$ films prepared on α-Al_2O_3 (001) single-crystal substrates by pulsed laser deposition. Note that its electrical conductivity is 0.063 S cm^{-1} at room temperature. The Mg-doped $CuCrO_2$ delafossite compound has the largest conductivity of 220 S cm^{-1}, but the optical transparency near 500 nm is limited in the range of 30–40%, and the conductivity is reduced from 200 to about 1 S cm^{-1} with improving the transparency.[12] Götzendörfer *et al.* also studied the $CuCrO_2$ and $CuAl_{0.5}Cr_{0.5}O_2$ films prepared by the

Key Laboratory of Polar Materials and Devices, Ministry of Education, Department of Electronic Engineering, East China Normal University, Shanghai 200241, People's Republic of China. E-mail: zghu@ee.ecnu.edu.cn; Fax: +86 21 54345119; Tel: +86 21 54345150

sol–gel method, and found that the conductivity (0.091 S cm^{-1}) and transmittance (49%) of the $CuAl_{0.5}Cr_{0.5}O_2$ film are superior to that of the $CuCrO_2$ film (0.063 S cm^{-1} and 21%, respectively).[13] In addition, the $CuCrO_2$ film has the lower synthesis temperature about 600 °C,[14] and the favorable thermal stability up to 1000 °C in air among the delafossite films.[15] Hence, one can expect that the $CuGa_{1-x}Cr_xO_2$ films have the combining advantages of lower resistivity and higher optical transparency, lower synthesis temperature, and the excellent thermal stability.

Due to the instability of Cu^{1+} and the sensibility of the oxygen partial pressure, most delafossite films have been prepared by vacuum based technologies, such as pulsed laser deposition and sputtering.[11,16] There are only some reports on the sol–gel synthesis of the delafossite films in recent years.[17–19] It should be noted that the preparation of $CuGaO_2$ film is more difficult than that of $CuAlO_2$ film owing to evaluation of thermodynamic and kinetic stability.[20] However, the sol–gel technique offers a high flexibility regarding material composition and the introduction of dopants because of its variability of stoichiometry. It is also a widely used industrial technique in numerous large scale production lines.[14] Recently, we have successfully synthesized the $CuGaO_2$ films by the sol–gel method.[21] The microstructure, phonon modes, optical properties, and electronic band structures of $CuGaO_2$ epitaxial films at different temperature ranges have been discussed. Nevertheless, in order to further optimize the material/device performances, the growth and physical properties of $CuGa_{1-x}Cr_xO_2$ system due to the Cr-introduction are still the open issues.

In this study, solid solution $CuGa_{1-x}Cr_xO_2$ ($0 \leq x \leq 1$) films were prepared by the sol–gel method. The microstructural, optical properties, electronic structures, and electrical transport properties have been systematically discussed. It was found that the Cr-substituting induced the change of the film microstructure. The optical transmittance of the films approach about 60–80% in the visible region. The new energy state was observed in the $CuGa_{0.8}Cr_{0.2}O_2$ film, with the highest electrical conductivity of 0.071 S cm^{-1} at room temperature among the $CuGa_{1-x}Cr_xO_2$ films.

2 Experimental

2.1 Chemical

Gallium(III) nitrate hydrate [$Ga(NO_3)_3 \cdot 5.97H_2O$, 99.9%], chromium(III) nitrate hydrate [$Cr(NO_3)_3 \cdot 9H_2O$, 99%] and copper(II) acetate hydrate [$Cu(AcO)_2 \cdot H_2O$, 99%] were used as raw materials with, anhydrous ethanol [C_2H_6O, 99.7%] and ethylene glycol [$C_2H_6O_2$, 99.0%] as solvent. All of the chemical reagents used in this experiment were of analytical grade without any further purification.

2.2 The fabrication of $CuGa_{1-x}Cr_xO_2$ ($0 < x \leq 1$) films

The $CuGa_{1-x}Cr_xO_2$ ($0 < x \leq 1$) sol was synthesized as follows: 2.5459 g gallium nitrate hydrate were dissolved in a mixture solvent (35 ml) of anhydrous ethanol and ethylene glycol with magnetic stirring, in which the content of anhydrous ethanol and ethylene glycol was 30 and 5 ml, respectively. After the solution was stable and became transparent and homogeneous, copper acetate hydrate (1.3975 g) was added into the solution. Stirring was continuous until copper acetate was completely dissolved, yielding a blue colored solution. Concurrently 2.8010 g chromium nitrate hydrate also were dissolved in a mixture solvent (35 ml) of anhydrous ethanol (30 ml) and ethylene glycol (5 ml) with magnetic stirring, and 1.3975 g copper acetate hydrate was added into the solution after it was stable, yielding a dark blue colored solution. Two solutions were mixed with different volume ratios, the obtained solutions of the $CuGa_{1-x}Cr_xO_2$ were all 10 ml, and 0.0611 g ethanolamine (C_2H_7NO, 99%) as additive was added, then the magnetic stirring was carried out again for 2 h. Note that the $[C_2H_7NO]/[Cu^{2+}]$ molar ratio of solutions was 1 : 2. The solutions were obtained as precursors for film deposition.

Prior to the deposition, the sapphire substrates were cleaned through nitric acid, deionized water, acetone and ethanol with ultrasonic cleaner sequentially. Then the transparent and homogeneous precursors were spin-coated onto (001) sapphire substrates at a speed of 4000 rpm for 20 s. The deposited films were preheated at 300 °C for 5 min in air to evaporate the solvent and remove organic residues in a rapid thermal processing. In order to obtain the films with desired thickness, the above process (spin-coating and preheating) was repeated six times. Finally, the films were annealed at 800 °C for 30 min in N_2 with a flow of 2.5 L min^{-1}.

2.3 The growth of $CuGaO_2$ films

The synthesis of the copper gallium sol was already described elsewhere.[21] 1.4552 g gallium nitrate hydrate was dissolved in anhydrous ethanol (20 ml) with magnetic stirring. After the solution was stable, copper acetate hydrate (0.7985 g) was added into the solution. Stirring was continuous until copper acetate was completely dissolved. Then 0.0611 g ethanolamine was added into the mixed solution, the $[C_2H_7NO]/[Cu^{2+}]$ molar ratio of the solution was 1 : 4. The magnetic stirring was carried out again for 2 h, yielding a blue colored precursors solution for film deposition. The sample preparation were the same to the preparation of the $CuGa_{1-x}Cr_xO_2$ ($0 < x \leq 1$) films. However, the viscosity coefficient of anhydrous ethanol is lower than that of ethylene glycol. To obtain a similar thickness to other films for the $CuGaO_2$ film, the above process (spin-coating and preheating) was repeated eight times. Finally, the films were annealed at 900 °C for 30 min in N_2 with a flow of 2.5 L min^{-1}.

2.4 Characterization methods

The crystalline structure of the $CuGa_{1-x}Cr_xO_2$ ($0 \leq x \leq 1$) films was analyzed by X-ray diffraction (XRD) using Cu Kα radiation (D/MAX-2550 V, Rigaku Co.). In the XRD experiments, a vertical goniometer (model RINT2000) was used, and continuous scanning mode ($2\theta/\theta$) was selected with an interval of 0.02° and the scanning rate of 10° min^{-1}. The cross-section microstructure of films were characterized using a scanning electron microscope (SEM, S-3000N, Philips XL30FEG). Raman scattering experiments were carried out by a micro-Raman spectrometer (Jobin-Yvon LabRAM HR 800 UV) with a 488 nm Ar^+ laser as the excited light. The X-ray photoelectron spectroscopy (XPS) experiments were carried out on a RBD upgraded PHI-5000C ESCA system (Perkin Elmer) with Mg Kα radiation ($h\nu$ = 1253.6 eV). The transmittance spectra were recorded by a

double beam ultraviolet-infrared spectrophotometer (Perkin Elmer UV/VIS Lambda 950) at the photon energy of 2650–190 nm (0.5–6.5 eV) with the interval of 2 nm at room temperature. Due to the high resistance values, it was impossible to resort to the four point measurement. Thus, the two point measurement was applied in the present work. Firstly, the electrodes of Pt were sputtered on both ends of the well-defined rectangle samples for ohmic contact. Then, the outgoing wires of electrodes were fixed with silver paste after a drying step. The sample was mounted into a Linkam THMSE 600 heating stage for variable temperature experiments from 125 to 423 K. The temperature can be controlled within the accuracy of 0.1 K. The possible oxidation of the device during the heating and cooling process can be avoided under a nitrogen atmosphere. A Keithley 2400 source meter was applied to provide an external direct-current voltage to the sample *via* Pt electrodes, and the resistance value can be recorded. Hall measurements were made by the Van der Pauw method at room temperature, which confirm the p-type behavior of the $CuGa_{1-x}Cr_xO_2$ films.

3 Results and discussion

3.1 Structural analysis

The XRD patterns of the $CuGa_{1-x}Cr_xO_2$ ($0 \leq x \leq 1$) films prepared on (001) sapphire substrates are shown in Fig. 1. As can be seen, all films exhibit a single phase with the rhombohedral (space group $R\bar{3}m$) structure. Besides the conspicuous (00*l*) diffraction peaks, some other peaks (012), (104), and (110) can also be found, illustrating that the films are polycrystalline with different orientations. Compared with stronger (012) orientation of the $CuCrO_2$ ($x = 1$) film, the $CuGaO_2$ ($x = 0$) film shows preferentially orientation along the *c*-axis perpendicular to the substrate surface, which is due to the well-defined epitaxial match with the (001) sapphire substrate and the higher preparation temperature. Because $CuGaO_2$ and $CuCrO_2$ are the isostructural delafossite compounds, the difference of the XRD patterns can be hardly seen, except for the tiny shift in peaks due to the difference of ionic radiuses ($r_{Cr} = 0.52$ Å, $r_{Ga} = 0.62$ Å). The positions of the (006) diffraction peak are estimated to be about 31.497° for $CuGaO_2$ and 31.515° for $CuCrO_2$ from 2θ angle measurements.

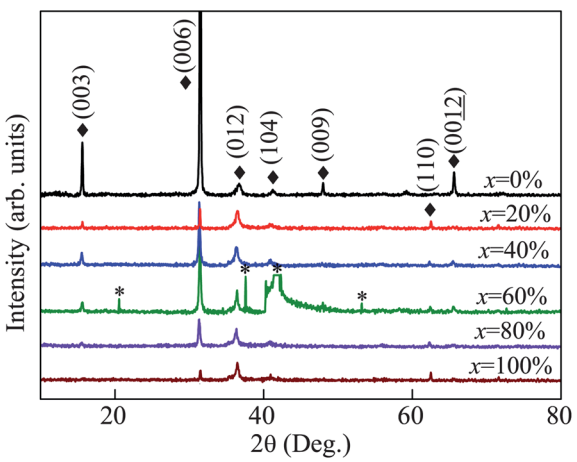

Fig. 1 XRD patterns of the $CuGa_{1-x}Cr_xO_2$ ($0 \leq x \leq 1$) films on (001) sapphire substrates. Note that the symbol (*) indicates the observed trace of the sapphire substrate.

Generally, the XRD pattern is frequently used to estimate the crystalline size and lattice parameter of the material.[14,21] The unit cell parameters are calculated to be about $a = 2.975$ Å, $c = 17.035$ Å for $x = 0$ ($CuGaO_2$) and $a = 2.969$ Å, $c = 17.034$ Å for $x = 1$ ($CuCrO_2$). The fact that the *c* parameter of the $CuCrO_2$ film is similar with that of the $CuGaO_2$ film indicates the increase of the Cu–O bond length in the $CuCrO_2$ film, due to the smaller ionic radius of Cr than that of Ga. The crystalline size can be calculated from the (006) peak according to the well-known Scherrer equation: $D = 0.9\lambda/(\beta\cos\theta)$, where $\lambda = 1.540$ Å is the average wavelength of Cu Kα radiation, $\beta^2 = (\mathrm{FWHM})^2 - b^2$, FWHM is the full width at half-maximum, *b* is a factor to compensate for the line broadening effect, and θ is the diffraction angle.[22] The calculated crystalline sizes are 47.7, 43.8, 30.7, 21.9, 29.9, and 39.1 nm with increasing *x* for the $CuGa_{1-x}Cr_xO_2$ ($0 \leq x \leq 1$) films, respectively. The smaller crystalline size indicates that there are more grain boundaries and the total amount of non-recombination centers inside films increases. Therefore, the Cr–Ga substituting with each other in the $CuGa_{1-x}Cr_xO_2$ ($0 < x < 1$) films induces more crystal defects and grain boundaries. It also indicates that the pure $CuGaO_2$ and $CuCrO_2$ films have relatively few grain boundaries and crystal defects. Note that the $CuGa_{0.4}Cr_{0.6}O_2$ sample shows some substrate peaks in Fig. 1, which may be due to the slight deviation between the cutting direction and (001) orientation of the sapphire crystal. Nevertheless, the discrepancy cannot affect the crystalline quality of the $CuGa_{1-x}Cr_xO_2$ films, as discussed in the following.

The surface and cross-sectional SEM images of the $CuGa_{1-x}Cr_xO_2$ films are shown in Fig. 2a–f for $x = 0$, 0.2, 0.4, 0.6, 0.8, and 1, respectively. From the surface images, the $CuGaO_2$ film has a surface pattern which is quite distinct from the $CuCrO_2$ film. For the $CuGaO_2$ film, the grains are closely gathered and densely arranged. There are no gaps among grains except for a few defects in the surface. The $CuCrO_2$ film is constituted by the regular and often hexagonal shaped particles, as can be seen in Fig. 2f. In addition, the surface pattern is gradually changed with increasing *x* for the $CuGa_{1-x}Cr_xO_2$ films. For the $CuGa_{0.8}Cr_{0.2}O_2$ and $CuGa_{0.6}Cr_{0.4}O_2$ films, the gaps increase with the Cr-substituting and particle boundaries become increasingly distinct. It is found that the Cr-substituting induced more crystal defects and grain boundaries. For $x > 0.5$, the films are constituted by particles, which become more and more regular with increasing *x*. These characteristics are also proved by the cross-sectional images. From the cross-sectional images, the $CuGaO_2$ and $CuGa_{1-x}Cr_xO_2$ films have the similar thickness with the distinct interface between film and sapphire substrate. However, the thickness of the $CuGa_{1-x}Cr_xO_2$ films slightly increases as the level of Cr-substituting is increased. It is because that the $CuCrO_2$ film is of a loose texture and the particle structure. Obviously, the Cr-substituting for the $CuGa_{1-x}Cr_xO_2$ films induces the increase of the film roughness, and changes the film internal structure.

3.2 Raman scattering

The delafossite compound is characterized by rhombohedral symmetry with the point group $3m$ (C_{3v}) and the space group

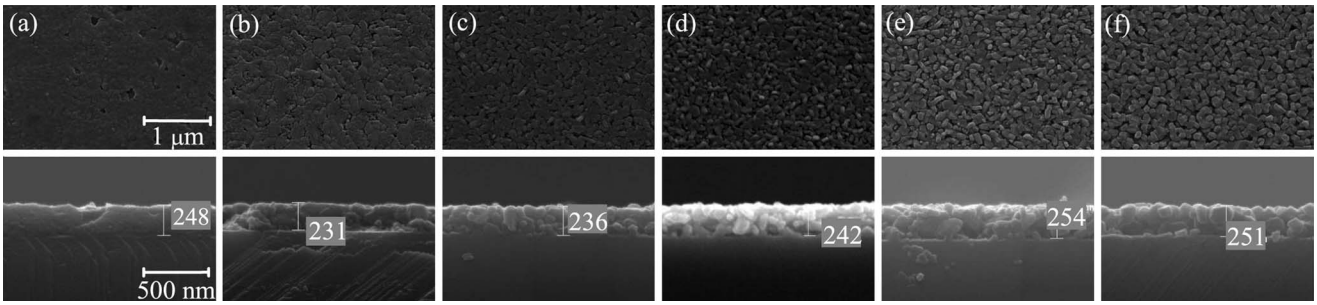

Fig. 2 The surface and cross-sectional SEM images of the $CuGa_{1-x}Cr_xO_2$ films for $x = 0$ (a), 0.2 (b), 0.4 (c), 0.6 (d), 0.8 (e) and 1 (f), respectively. Note that the different scales are given in the pictures.

$R\bar{3}m$ (C_{3v}^6), with four atoms in the primitive cell, which gives rise to 12 normal modes.[23] According to the group theory, a general mode at the Brillouin zone center as $\Gamma = A_{1g} + E_g + 3A_{2u} + 3E_u$, out of which A_{1g} and E_g symmetry are Raman active.[24] Fig. 3 shows the Raman spectra of the $CuGa_{1-x}Cr_xO_2$ ($0 \le x \le 1$) films using a 488 nm laser at the room temperature. There is the pure delafossite phase and no cubic spinel phase or CuO impurities are detected. Note that the traces of the sapphire substrate are observed only in the $CuGaO_2$ film because of the higher optical transparency near 488 nm than that of other films (the optical properties will be discussed in the 3.4 part). In addition, the Cr^{3+} ions are coordinated octahedrally in the delafossite lattice, the energy level of their partially filled 3d shell will split into two levels according to the ligand field theory. The excitation of electrons from the lower to the upper of these two levels could happen by absorbing the photons in the visible range, which further induces the coloration for the films with a higher Cr composition.[14,17] Therefore, the excitation light used in Raman experiment cannot reach the substrate for the samples including Cr^{3+} ions. In order to obtain the A_{1g} phonon mode of the $CuGaO_2$ film, the Lorentz multi-peaks fitting was used in the frequency range from 678 to 804 cm^{-1}. Therefore, for the $CuGaO_2$ film, the Raman scattering peaks were observed around 104 (E_u), 213 (A_g), 377 (E_g) and 738 (A_{1g}) cm^{-1}, which agree well with earlier calculation results on those compounds with delafossite structure.[23] The Raman scattering peaks of the $CuCrO_2$ film are around 97 and 105 (E_u), 205 (A_g), 454 (E_g) and 707 (A_{1g}) cm^{-1}, also according with the result of Amami *et al.*[25]

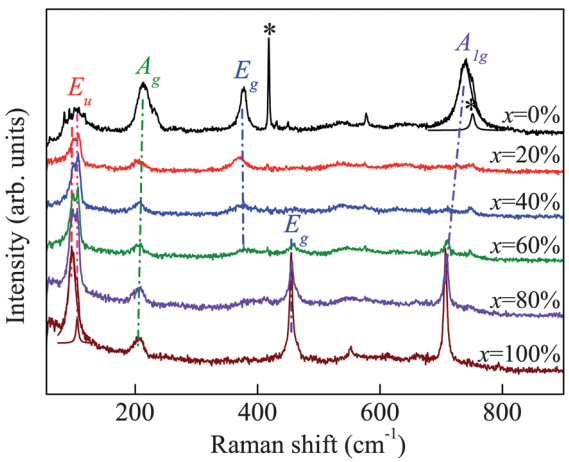

Fig. 3 Raman spectra of the $CuGa_{1-x}Cr_xO_2$ ($0 \le x \le 1$) films under the excitation line of 488 nm. Note that the dash–dot lines show the positions of Raman-active phonon modes and the symbol (*) indicates the observed trace from the sapphire substrate.

Obviously, the peak positions of the A_g and A_{1g} phonon modes shift toward a lower frequency side with increasing x for the $CuGa_{1-x}Cr_xO_2$ films, especially for the A_{1g} phonon mode. The A_g and A_{1g} phonon modes imply the atomic vibrations in the direction of the Cu–O bonds, along the hexagonal c-axis. Hence, the shift indicates that the interatomic potential becomes weaker between Cu and O atoms with increasing x, owing to the Cu–O bond length increasing with the Cr composition. The increase of the Cu–O bond length in the $CuCrO_2$ film is also proved from the XRD patterns. From the Raman spectra, there is an evident discrepancy of the positions for the E_g phonon mode between the $CuGaO_2$ and $CuCrO_2$ films. The double degenerate E_g mode describes the vibration in the perpendicular direction along the c-axis. Hence, the vibration along the a-axis is strictly different from the $CuGaO_2$ and $CuCrO_2$ films. The intensity of the E_g peak for the $CuGaO_2$ film becomes weaker with increasing x, while the intensity of the E_g peak for the $CuCrO_2$ film continuously increases. However, the positions of the E_g peak are nearly unchanged. Interestingly, the infrared-active mode of the E_u peak is observed due to the structural distortions. The E_u phonon mode is constituted of two peaks in the solid solution $CuGa_{1-x}Cr_xO_2$ films, except for the $CuGaO_2$ film. It is because the $CuGaO_2$ film has the better crystallization and fewer defects than other films, confirmed by the XRD and SEM images. The difference between the E_u peaks is smaller in the $CuCrO_2$ film than that from the other films. It indicates that the Cr–Ga substituting with each other makes the structure distortion of the crystal lattice aggravated.

3.3 XPS of the $CuGa_{1-x}Cr_xO_2$ films

Elemental compositions and chemical states of the $CuGa_{1-x}Cr_xO_2$ ($0 \le x \le 1$) films were studied by XPS measurements. The survey spectra for all films indicate that only C 1s, Cu 2p, Ga 3d and 2p, Cr 2p, O 1s, and N 1s related core levels can be detectable. The C 1s peak at 284.6 eV is used as an internal standard, and the other spectra are calibrated with the C 1s peak to correct the binding energy position. For example, high resolution spectra of Ga 3d and 2p and Cr 2p for the $CuGa_{0.6}Cr_{0.4}O_2$ film are shown in Fig. 4. The peaks at binding energies of 932.5 eV (Cu $2p_{3/2}$) and 952.1 eV (Cu $2p_{1/2}$) for the

$CuGa_{0.6}Cr_{0.4}O_2$ film with a spin-orbit splitting of 19.6 eV can be observed in Fig. 4a, where Cu ions have a +1 valence state, which is in good agreement with the findings in the core level spectra of $CuFeO_2$ and $CuAlO_2$ films.[24,26] Note that there is no shake-up line of Cu $2p_{3/2}$ in the spectrum. It is well established that the core level spectrum of Cu^{2+} compounds has a strong satellite feature (shake-up satellite) which is absent in the core level spectra of Cu^{1+} compounds.[27] This feature has been widely used for the identification of different oxidation states of copper in various copper compounds. XPS studies along with XRD and Raman results indicate that there is the single phase in the present $CuGa_{1-x}Cr_xO_2$ films.

Fig. 4b shows the N 1s XPS spectra of the $CuGa_{1-x}Cr_xO_2$ (x = 0, 0.4, 1) films. It is also important to note that N 1s peaks are located at 396.4–397.5 eV, which is in good agreement with the data of N-doped $CuCrO_2$ and $CuAlO_2$ films.[28,29] Combining with the above mentioned XRD, Raman and XPS results, it is concluded that the nitrogen atoms have been incorporated into the $CuGa_{1-x}Cr_xO_2$ films. The binding energies of Cu 2p, Ga 3d and 2p, Cr 2p, and O 1s were found to be unchanged regardless of the amount of nitrogen element. In addition, no bonding has occurred between Cu–N, Ga–N, Cr–N, and O–N. Thus, nitrogen atoms can be readily fitted in the interstitial sites of the crystal $CuGa_{1-x}Cr_xO_2$ structure. The detailed composition of the $CuGa_{1-x}Cr_xO_2$ films including nitrogen element are listed in Table 1. The effect of the N-doping will be discussed in the last paragraph of section 3.4. However, the origin of N-doping may be from the precursor because the ethanolamine includes nitrogen element. It may be also induced by the diffusion because that the present $CuGa_{1-x}Cr_xO_2$ films were annealed in N_2 flow of 2.5 L min^{-1}.

The Ga 3d and 2p XPS spectra of $CuGa_{0.6}Cr_{0.4}O_2$ were observed at 19.1, 21.3, and 1118.0 eV for $3d_{5/2}$, $3d_{3/2}$, and $2p_{3/2}$ peaks, respectively, as shown in Fig. 4c. The Cr 2p XPS spectra of $CuGa_{0.6}Cr_{0.4}O_2$ were observed at 576.7 and 586.4 eV for $2p_{3/2}$ and $2p_{1/2}$ peaks in Fig. 4d. The XPS data suggest that both Ga and Cr ions are in +3 electronic state. The detailed amounts of Ga and Cr in the $CuGa_{0.6}Cr_{0.4}O_2$ film are listed in Table 1, the Ga/Cr atomic ratio is about 3 : 2. In addition, the deconvolution of the O 1s XPS spectra for the $CuGa_{1-x}Cr_xO_2$ films are fitted by two components.[30,31] One of the O 1s peaks located at 530.3 eV for all films is ascribed to the lattice oxygen of the $CuGa_{1-x}Cr_xO_2$ films. While the higher binding energy peak about 531.7 eV in O 1s for the $CuGa_{1-x}Cr_xO_2$ films reveals the presence of the chemisorbed O-containing species. The relatively high intensity of the "O_{chem}" component is due to the very good surface sensitivity. Table 1 shows the compositions of the $CuGa_{1-x}Cr_xO_2$ films based on the experimental and fitted XPS peak areas and the sensitivity factors. It can be seen that the composition of Ga is decreasing while the composition of Cr is increasing with increasing x. The Ga/Cr atomic ratios are in good agreement with the stoichiometric ratios of the precursors.

Table 1 Compositions of the $CuGa_{1-x}Cr_xO_2$ films as determined from XPS measurements

	XPS atomic concentration (at%)				
Sample	Cu	Ga	Cr	O	N
x = 0%	24.4	24.1	—	50.5	0.98
x = 10%	23.5	21.6	2.22	50.4	2.28
x = 20%	23.3	18.6	4.98	50.4	2.72
x = 40%	23.9	14.3	9.79	49.0	3.01
x = 60%	24.2	9.54	14.1	49.4	2.77
x = 80%	23.5	5.19	19.0	49.0	3.31
x = 100%	23.3	—	26.3	47.1	3.28

3.4 Optical properties and electronic structures

The optical transmission spectra of the $CuGa_{1-x}Cr_xO_2$ ($0 \le x \le 1$) films were measured, as shown in Fig. 5. The spectra can be roughly separated into two photon energy regions: a ultraviolet-visible one (labeled with "I"), and a near infrared one ("II"). From the view of transmittance, the $CuGa_{1-x}Cr_xO_2$ films have the high near-infrared transmittance (about 80%) in region II. In region I, however, the visible optical transmittance of the $CuGa_{1-x}Cr_xO_2$ films approach about 60–80%, which is a very

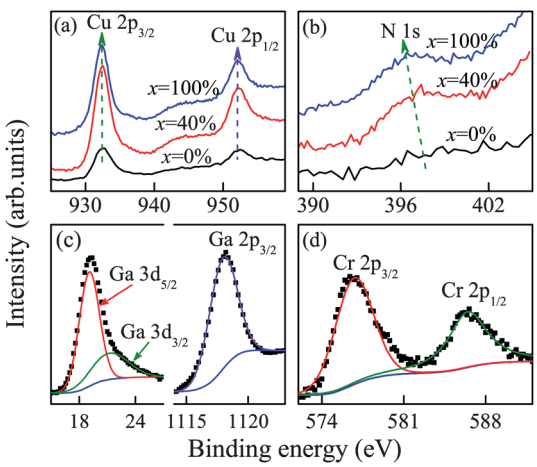

Fig. 4 XPS spectra of the (a) Cu 2p and (b) N 1s regions for the $CuGa_{1-x}Cr_xO_2$ (x = 0, 0.4, 1) films, (c) Ga 3d and 2p and (d) Cr 2p regions for the $CuGa_{0.6}Cr_{0.4}O_2$. Note that the dotted and solid lines in (c) and (d) indicate the experiment data and fitting results, respectively.

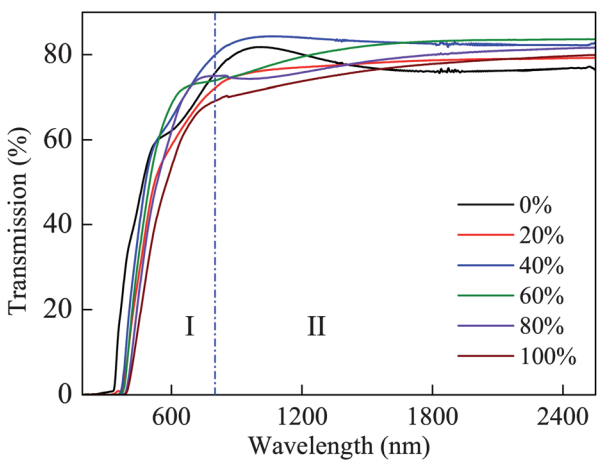

Fig. 5 Transmission spectra of the $CuGa_{1-x}Cr_xO_2$ ($0 \le x \le 1$) films. Note that the spectra were separated into two photon energy regions: a ultraviolet-visible one (labeled with "I"), and a near infrared one ("II").

important parameter for applications, as one of the criteria for the selection of TCOs. The $CuGaO_2$ film has the steepest absorption edge relative to the other films. The $CuCrO_2$ film has the lowest visible optical transmittance and the gentlest absorption edge. Note that the absorption edge of the other films shifts between the $CuGaO_2$ and $CuCrO_2$ films.

The optical band gap, E_{OBG} is deduced by Tauc's relation $(\alpha h\nu)^n = A(h\nu - E_{OBG})$, α denotes the absorption coefficient obtained by the relation, $\alpha = -\ln(T)/d$, where d is the layer thickness, and T is the transmittance of the layers.[32,33] The nature of the band gap is identified by the exponent n and an intercept of the $(\alpha h\nu)^n$ plot with photon energy, $h\nu$ yields the optical band gap energy. Fig. 6a and b display the $(\alpha h\nu)^n$ *versus* $h\nu$ plots, with $n = 2$ for direct band gap (E^{dir}_{OBG}) and $n = 1/2$ for indirect band gap (E^{indir}_{OBG}) transitions of the $CuGa_{1-x}Cr_xO_2$ ($0 \le x \le 1$) films, respectively. In Fig. 5a, the direct optical band gaps for the $CuGa_{1-x}Cr_xO_2$ films are 3.56, 3.34, 3.28, 3.18, 3.13, and 3.09 eV with increasing x, respectively. Obviously, the values of the direct band gap linearly decrease with increasing x, which can be written as $E^{dir}_{OBG}(x) = (1-x)E^{dir}_{CuGaO2} + xE^{dir}_{CuCrO2}$. In Fig. 6b, the indirect band gaps of the $CuGa_{1-x}Cr_xO_2$ films are 3.24, 2.88, 2.83, 2.78, and 2.72 eV for $x = 0$, 0.4, 0.6, 0.8, and 1, respectively. For the delafossite $CuMO_2$ (M = Al, Ga, In) compounds, Nie *et al.*[34] and Huda *et al.*[35] have discussed the fact that they all have the indirect character of the band gap, but the indirect transition is weaker compared with the direct transition, due to the direct transition playing a dominant role in the spectral response. It was discussed and proved in the recent paper.[21] Lim *et al.* also reported that the direct and indirect optical band gaps of the Mg-doped $CuCrO_2$ film prepared by the chemical spray pyrolysis are 3.11 and 2.58 eV, respectively.[36]

Note that the E^{indir}_{OBG} band gap of the $CuGa_{0.8}Cr_{0.2}O_2$ film cannot be derived because there is a new and strong energy level near the valence band edge in the film. The value between the new energy level and the conduction band is calculated about 3.17 eV, as shown in Fig. 7a. On the other hand, the new band gap located at 0.17 eV above the top of the valence band is observed in the $CuGa_{0.8}Cr_{0.2}O_2$ film, as shown in Fig. 8. Hence, it can be considered that the electrons are easily excited out of the filled valence band and jump into the new energy level. Then, the holes in the valence band are increased and contribute to the electrical conductivity. The statement will be further discussed in the latter electrical transport experiments. Moreover, the similar energy state is also discovered in the $CuGa_{0.9}Cr_{0.1}O_2$ and $CuGa_{0.75}Cr_{0.25}O_2$ films, as shown in Fig. 7b. Note that the new energy state becomes weaker with increasing the Cr composition.

The new energy level is also observed in the $CuCrO_2$ and $CuAlO_2$ films.[28,29] They ascribed the origin of the new energy state to the interstitial nitrogen, which provided an impurity energy level in the energy gap. Because the present $CuGa_{1-x}Cr_xO_2$ films were annealed in N_2 flow of 2.5 L min^{-1} and the ethanolamine in the precursors also includes the nitrogen element, the detailed evaluation of the compositions is necessary. The chemical compositions of the $CuGa_{1-x}Cr_xO_2$ films are analyzed by X-ray photoelectron spectra, as previously presented in Table 1. The results show that there are nitrogen element in all the films. The compositions of nitrogen element for the $CuGa_{1-x}Cr_xO_2$ ($0.4 \le x \le 1$) films is nearly similar to that of the $CuGa_{1-x}Cr_xO_2$ ($0.1 \le x \le 0.2$) films. However, the new energy level is not found in the $CuGa_{1-x}Cr_xO_2$ ($0.4 \le x \le 1$) films. Hence, the new energy level may be not induced by the nitrogen because the characteristic is only observed for $0 < x \le 0.25$. Nevertheless, it becomes weaker with increasing x. Therefore, the new energy level may be the defect energy level induced by the Cr-substituting. The XRD patterns and SEM images also indicate that there are relatively more number of grain boundaries and crystal imperfections of the $CuGa_{1-x}Cr_xO_2$ films than that of the pure $CuGaO_2$ and $CuCrO_2$ films. Moreover, both Ga and Cr are trivalent elements in the solid solution $CuGa_{1-x}Cr_xO_2$ films. No other impurity phase is found in the XRD patterns and Raman spectra for the $CuGa_{1-x}Cr_xO_2$ films. It is confirmed that the new energy state cannot originate from the impurity level once again. Yu *et al.* reported that the Hall mobility was decreased with increasing nitrogen composition.[28] The result confirms the fact that the new energy state was the defect energy level. The N-doping induced the form of the crystal defects, the overdoping can result in the more crystal defects, which form the

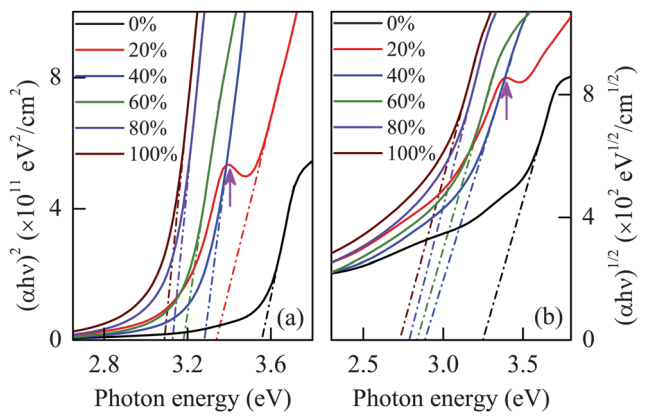

Fig. 6 (a) Plots of $(\alpha h\nu)^2$ *vs.* the photon energy for the estimation of direct optical band gap energies from the $CuGa_{1-x}Cr_xO_2$ ($0 \le x \le 1$) films. (b) Plots of $(\alpha h\nu)^{1/2}$ *vs.* the photon energy for the estimation of indirect band gap energies from the $CuGa_{1-x}Cr_xO_2$ ($0 \le x \le 1$) films. Note that the arrow indicates that there is a new energy state in the band gap of the $CuGa_{0.8}Cr_{0.2}O_2$ film.

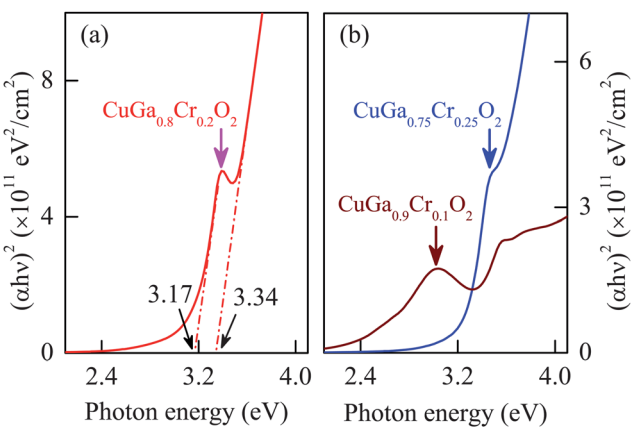

Fig. 7 Plots of $(\alpha h\nu)^2$ *vs.* the photon energy for the evaluation of direct optical band gap values from the films corresponding to (a) $CuGa_{0.8}Cr_{0.2}O_2$, (b) $CuGa_{0.75}Cr_{0.25}O_2$ and $CuGa_{0.9}Cr_{0.1}O_2$ films, respectively.

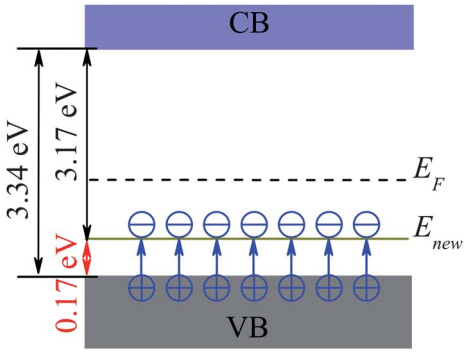

Fig. 8 Schematic representation of the electronic band structure for the $CuGa_{0.8}Cr_{0.2}O_2$ films, where E_F and E_{new} denote the Fermi energy level and the new energy level, respectively. Note that the symbols (⊕) and (⊖) indicate the hole and electron, respectively.

defect energy level. It was also improved by Dong *et al.* because that they discovered the new energy state for the film deposited with 30 vol% N_2O, but the new energy state was not found for the films deposited with 10 and 20 vol% N_2O.[29] Correspondingly, the new energy level may be induced by the crystal defects.

3.5 Electrical transport

To further understand the intrinsic characteristics of the $CuGa_{1-x}Cr_xO_2$ ($0 \le x \le 1$) films, the temperature dependence of electrical conductivity is shown in Fig. 9. It is evident that there is a semiconductive temperature dependence. As can be seen in plots of ln σ *vs.* $1000/T$ (Fig. 9a), the $CuGa_{1-x}Cr_xO_2$ films show a thermal activation behavior at high temperature. So the conductivity of films at high temperature can be expressed by $\sigma = A_{exp}(-E_a/k_BT)$, where E_a is the thermal activation energy, k_B is Boltzmann constant, and A is a constant. The estimated E_a values are 210, 175, 222, 252, 284, and 321 meV for $x = 0$, 0.2, 0.4, 0.6, 0.8, and 1, respectively. A continuous increment in the E_a values with increasing x was clearly observed, except for the $CuGa_{0.8}Cr_{0.2}O_2$ film. It has the lowest value of the thermal activation energy and the largest electrical conductivity, which may be due to the new energy level located above the top of the valence band. The appearance of the new energy level induces the increase of the hole in the valence band, and contributes to the electrical conductivity. As can be seen in Fig. 9a and b, the crossover is about 200 K in the $CuGa_{0.8}Cr_{0.2}O_2$ film from thermal activation behavior to that of three-dimensional variable range hopping as expressed by $\ln \sigma \propto T^{-1/4}$ occurs. The crossover was previously observed in $CuAlO_2$ (ref. 9), $CuGaO_2$ (ref. 11), and $CuCrO_2$ films.[37] In the high temperature region, the hopping of holes between the nearest-neighbor Cu sites may determine the electrical transport properties. In the lower temperature region, the decrease of the thermal energy may depress the hopping between the nearest-neighbor Cu sites. The contribution of the hopping to the Ga and Cr sites becomes prominent. Hence, the hopping to the Cu site in the other Cu layers becomes relatively dominant so that the conductivity shows the three-dimensional variable range-hopping behavior.[38]

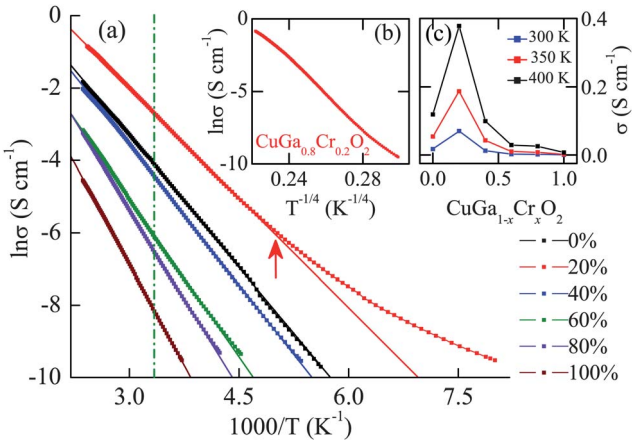

Fig. 9 (a) Plots of ln σ *vs.* $1000/T$ of the $CuGa_{1-x}Cr_xO_2$ ($0 \le x \le 1$) films, and the linear fit of each curve determines the activation energy E_a, where the dash–dot line shows the point of 300 K. The inset of (b) shows the ln σ *vs.* $T^{-1/4}$ plot of the $CuGa_{0.8}Cr_{0.2}O_2$ film, indicating that the three-dimensional variable range hopping mechanism becomes dominant for the sample. The inset of (c) shows the electrical conductivity of the $CuGa_{1-x}Cr_xO_2$ ($0 \le x \le 1$) films at 300, 350, and 400 K, respectively. Note that the arrow indicates the crossover at which the electric conductivity starts to deviate from the thermal activation behavior.

Let us shed light on the electrical conductivity σ. The electrical conductivity has the largest value of 0.071 S cm^{-1} for $x = 0.2$ at room temperature. It is slightly larger than that of the $CuGaO_2$ film (0.017 S cm^{-1}). However, it is two orders of magnitude larger than that of the $CuCrO_2$ film (0.0006 S cm^{-1}). The electrical conductivity change of the $CuGa_{0.8}Cr_{0.2}O_2$ film with the temperature is much more obvious than others, especially for the $CuCrO_2$ film. It is because that the $CuGa_{0.8}Cr_{0.2}O_2$ film has the lowest thermal activation energy. In addition, electrical transport properties of the $CuGa_{1-x}Cr_xO_2$ films were listed in Table 2, which were made by Van der Pauw Hall-test method at room temperature. As can be seen, the carrier concentration of the $CuGa_{0.8}Cr_{0.2}O_2$ film is one magnitude larger than that of the other films, which also indicates that the new energy level induced the increase of the hole in the valence band and contributed to the electrical conductivity. Although there are other reports on the fact that the doping of the divalent element (*e.g.*, Mg, Ca) greatly increases the electrical conductivity of the delafossite compound,[39,40] the $CuGa_{1-x}Cr_xO_2$ films in the present work are the undoping system prepared by the sol–gel method. One can think that the present $CuGa_{1-x}Cr_xO_2$ films have better physical properties, as compare to those reported up to now. Meanwhile, the visible optical transmittance of the $CuGa_{1-x}Cr_xO_2$ films approaches about 60–80%. Therefore, the

Table 2 Electrical transport properties of the $CuGa_{1-x}Cr_xO_2$ films at room temperature

Sample	Conductivity (S cm^{-1})	Carrier concentration (cm^{-3})	Hall mobility (cm^2 V^{-1} s^{-1})
$x = 0\%$	0.017	2.93×10^{16}	3.37
$x = 10\%$	0.033	9.54×10^{16}	2.15
$x = 20\%$	0.071	2.25×10^{17}	1.92
$x = 40\%$	0.013	2.84×10^{16}	2.79
$x = 60\%$	0.0024	7.29×10^{15}	2.18
$x = 80\%$	0.0017	2.19×10^{15}	5.05
$x = 100\%$	0.0006	2.91×10^{14}	14.3

present delafossite materials are of the better optical and electrical properties, and show the promising application values, especially for the $CuGa_{0.8}Cr_{0.2}O_2$ film.

4 Conclusions

In summary, we successfully prepared pure phase $CuGa_{1-x}Cr_xO_2$ ($0 \leq x \leq 1$) films on (001) sapphire substrates by the sol–gel method. The smaller ionic radiuses and the similar value of the *c* parameters indicated that the Cu–O bond length is increased in the $CuCrO_2$ film. Due to the interatomic potential becoming weaker between Cu and O atoms with increasing the Cu–O bond length, the peak positions of the A_{1g} and A_g phonon modes shifted toward a lower frequency with increasing *x*. The distortions of the crystal lattice were aggravated by the Cr–Ga substituting, which induced the E_u phonon mode constituted with two peaks in the $CuGa_{1-x}Cr_xO_2$ films. The visible optical transmittance of the $CuGa_{1-x}Cr_xO_2$ films approach about 60–80%. The values of the direct band gap linearly decrease with increasing *x*. The new energy level located above the top of the valence band was observed in the $CuGa_{0.8}Cr_{0.2}O_2$ film, which may be derived from the defect energy level. It induced the increase of the hole in the valence band, contributed to the electrical conductivity, and lowered the thermal activation energy. The $CuGa_{0.8}Cr_{0.2}O_2$ film had the largest electrical conductivity of 0.071 S cm^{-1} at room temperature, which makes it promising for applications in the optoelectronic field.

Acknowledgements

One of the authors (M.J.H) would like to thank Yuanyuan Liao for Raman scattering experiments and Zhipeng Huang for Hall measurements. This work was financially supported by Major State Basic Research Development Program of China (Grant no. 2011CB922200), Natural Science Foundation of China (Grant nos. 11074076, 60906046, and 61106122), Projects of Science and Technology Commission of Shanghai Municipality (Grant nos. 10DJ1400201, 10SG28, and 11520701300), and the Program for Professor of Special Appointment (Eastern Scholar) at Shanghai Institutions of Higher Learning.

References

1 Y. M. Kim, W. J. Lee, D.-R. Jung, J. M. Kim, S. H. Nam, H. C. Kim and B. W. Park, *Appl. Phys. Lett.*, 2010, **96**, 171902.
2 F. Yang and S. R. Forrest, *Adv. Mater.*, 2006, **18**, 2018–2022.
3 H. M. Luo, M. K. Jain, T. M. McCleskey, E. Bauer, A. K. Burrell and Q. X. Jia, *Adv. Mater.*, 2007, **19**, 3604–3607.
4 A. J. Chiquito, A. J. C. Lanfredi, R. F. M. de Oliveira, L. P. Pozzi and E. R. Leite, *Nano Lett.*, 2007, **7**, 1439–1443.
5 R. Jaramillo and S. Ramanathan, *Adv. Funct. Mater.*, 2011, **21**, 4068–4072.
6 C. Y. Zhang, X. M. Li, J. M. Bian, W. D. Yu and X. D. Gao, *Surf. Coat. Technol.*, 2005, **198**, 253–256.
7 F. Fang, D. X. Zhao, X. Fang, J. H. Li, Z. P. Wei, S. Z. Wang, J. L. Wu and X. H. Wang, *J. Mater. Chem.*, 2011, **21**, 14979–14983.
8 Ü. Özgür, Y. I. Alivov, C. Liu, A. Teke, M. A. Reshchikov, S. Doğn, V. Avrutin, S. J. Cho and H. Morkoc, *J. Appl. Phys.*, 2005, **98**, 041301.
9 H. Kawazoe, M. Yasukawa, H. Hyodo, M. Kurita, H. Yanagi and H. Hosono, *Nature*, 1997, **389**, 939.
10 D. O. Scanlon and G. W. Watson, *J. Mater. Chem.*, 2011, **21**, 3655–3663.
11 K. Ueda, T. Hase, H. Yanagi, H. Kawazoe, H. Hosono, H. Ohta, M. Orita and M. Hirano, *J. Appl. Phys.*, 2001, **89**, 1790–1793.
12 R. Nagarajan, A. D. Draeseke, A. W. Sleight and J. Tate, *J. Appl. Phys.*, 2001, **89**, 8022–8025.
13 S. Götzendörfer, R. Bywalez and P. Löbmann, *J. Sol-Gel Sci. Technol.*, 2009, **52**, 113–119.
14 R. Bywalez, S. Götzendörfer and P. Löbmann, *J. Mater. Chem.*, 2010, **20**, 6562–6570.
15 M. Lalanne, A. Barnabé, F. Mathieu and P. Tailhades, *Inorg. Chem.*, 2009, **48**, 6065–6071.
16 M. Fang, H. P. He, B. Lu, W. G. Zhang, B. H. Zhao, Z. Z. Ye and J. Y. Huang, *Appl. Surf. Sci.*, 2011, **257**, 8330–8333.
17 S. Götzendörfer, C. Polenzky, S. Ulrich and P. Löbmann, *Thin Solid Films*, 2009, **518**, 1153–1156.
18 Y. F. Wang, Y. J. Gu, T. Wang and W. Z. Shi, *J. Alloys Compd.*, 2011, **509**, 5897–5902.
19 A. Alias, M. Sakamoto, T. Kimura and K. Uesugi, *Jpn. J. Appl. Phys.*, 2012, **51**, 035503.
20 K. Yuh, H. Motohiro, K. Yuhki, E. Satoshi, O. Eri and H. Takuya, *J. Therm. Anal. Calorim.*, 2010, **99**, 57.
21 M. J. Han, K. Jiang, J. Z. Zhang, Y. W. Li, Z. G. Hu and J. H. Chu, *Appl. Phys. Lett.*, 2011, **99**, 131104.
22 X. Mathew, J. P. Enriquez, C. Mejía-García, G. Contreras-Puente, M. A. Cortes-Jacome, J. A. Toledo Antonio, J. Hays and A. Punnoose, *J. Appl. Phys.*, 2006, **100**, 073907.
23 J. Pellicer-Porres, A. Segura, E. Martínez, A. M. Saitta, A. Polian, J. C. Chervin and B. Canny, *Phys. Rev. B: Condens. Matter Mater. Phys.*, 2005, **72**, 064301.
24 S. P. Pavunny, A. Kumar and R. S. Katiyar, *J. Appl. Phys.*, 2010, **107**, 013522.
25 M. Amami, C. V. Colin, P. Strobel and A. Ben Salah, *Phys. B*, 2011, **406**, 2182–2185.
26 M. Fang, H. P. He, B. Lu, W. G. Zhang, B. H. Zhao, Z. Z. Ye and J. Y. Huang, *Appl. Surf. Sci.*, 2011, **257**, 8330–8333.
27 J. Ghijsen, L. H. Tjeng, J. van Elp, H. Eskes, J. Westerink and G. A. Sawatzky, *Phys. Rev. B*, 1988, **38**, 11322.
28 R. S. Yu, S. C. Liang, C. J. Lu, D. C. Tasi and F. S. Shieu, *Appl. Phys. Lett.*, 2007, **90**, 191117.
29 G. B. Dong, M. Zhang, X. P. Zhao, H. Yan, C. Y. Tian and Y. G. Ren, *Appl. Surf. Sci.*, 2010, **256**, 4121–4124.
30 W. L. Yu, W. W. Li, J. D. Wu, J. Sun, Z. G. Hu and J. H. Chu, *J. Appl. Phys.*, 2011, **110**, 123502.
31 H. Dong, Z. H. Li, X. M. Xu, Z. X. Ding, L. Wu, X. X. Wang and X. Z. Fu, *Appl. Catal., B*, 2009, **89**, 551–556.
32 H. Hiramatsu, W.-S. Seo and K. Koumoto, *Chem. Mater.*, 1998, **10**, 3033–3039.
33 Z. G. Hu, Y. W. Li, F. Y. Yue, Z. Q. Zhu and J. H. Chu, *Appl. Phys. Lett.*, 2007, **91**, 221903.
34 X. L. Nie, S.-H. Wei and S. B. Zhang, *Phys. Rev. Lett.*, 2002, **88**, 066405.
35 M. N. Huda, Y. Yan, A. Walsh, S.-H. Wei and M. M. Al-Jassim, *Phys. Rev. B: Condens. Matter Mater. Phys.*, 2009, **80**, 035205.
36 S. H. Lim, S. Desu and A. C. Rastogi, *J. Phys. Chem. Solids*, 2008, **69**, 2047–2056.
37 S. Mahapatra and S. A. Shivashankar, *Chem. Vap. Deposition*, 2003, **9**, 238–240.
38 T. Okuda, N. Jufuku, S. Hidaka and N. Terada, *Phys. Rev. B: Condens. Matter Mater. Phys.*, 2005, **72**, 144403.
39 B. J. Ingram, B. J. Harder, N. W. Hrabe, T. O. Mason and K. R. Poeppelmeier, *Chem. Mater.*, 2004, **16**, 5623–5629.
40 Z. H. Deng, X. D. Fang, R. H. Tao, W. W. Dong, S. Zhou, G. Meng and J. Z. Shao, *J. Alloys Compd.*, 2011, **509**, 5300–5304.

